

SCIENTIFIC REPORTS



OPEN

A general nonaqueous sol-gel route to g-C₃N₄-coupling photocatalysts: the case of Z-scheme g-C₃N₄/TiO₂ with enhanced photodegradation toward RhB under visible-light

Received: 06 September 2016

Accepted: 23 November 2016

Published: 22 December 2016

Xu Liu¹, Nan Chen², Yuxiu Li¹, Dongyang Deng¹, Xinxin Xing¹ & Yude Wang^{2,3}

The g-C₃N₄-coupling TiO₂ photocatalysts with controllable particle size as well as the interface contact were prepared by a general nonaqueous sol-gel method. The structural and morphological features of g-C₃N₄/TiO₂ were investigated through the X-ray diffraction, Fourier transformed infrared spectra, scanning electron microscopy and transmission electron microscopy, respectively. It is found the TiO₂ nanoparticles with a size of 7.3 ± 1.6 nm are uniformly anchored on the surface of the g-C₃N₄ nanosheets in isolation. The photocatalytic properties of as-prepared g-C₃N₄/TiO₂ were tested by degradation of Rhodamine B (RhB) under visible light, and an enhanced activity is observed. The mechanism of the enhanced activity was further investigated through N₂ adsorption-desorption isotherms, UV-vis spectra, photoluminescence spectra, photoelectrochemical measurements, radical trapping experiments and X-ray photoelectron spectroscopy. Furthermore, the photocatalytic performances of obtained g-C₃N₄/TiO₂ under sunlight were also evaluated in aspects of degradation efficiency and stability. The results indicate that the obtained g-C₃N₄/TiO₂ is one promising photocatalyst for practical applications. The study of as-prepared g-C₃N₄/TiO₂ also implies that the present method could be a general route of g-C₃N₄-coupling photocatalysts.

Facing energy depletion and environment pollution, the techniques utilizing inexhaustible sunlight to catalyze specific reactions, such as hydrogen production from water splitting^{1–3}, CO₂ reduction into hydrocarbon fuels^{4,5}, as well as decomposition of environmental pollutant attract numerous attentions^{6–10}. For these applications, the core is highly active photocatalysts which possess similar operation mechanisms including formation of photo-generated carries and corresponding redox reactions¹¹. Due to the mechanisms, the photocatalysts suffer from some inherent weaknesses. Specifically, wide-band catalysts can only utilize ultraviolet which only takes lower than 6% of the sunlight; visible-light catalysts possesses low redox ability; both of them suffer from the recombination of the photogenerated carries. One of the effective solutions is semiconductor coupling which seems a general route to get over the inherent weaknesses for both wide-band and visible-light photocatalysts¹². Through typical heterojunction charge transfer, the coupling of visible-light and wide-band photocatalysts endows wide-band catalyst better utilizations of visible light. On the other hand, through Z-scheme charge transfer, the coupling of visible-light photocatalysts can also realize stronger redox ability. No matter Z-scheme or typical heterojunction charge transfer, the possibility of carries recombination will be decreased. However, the formation of the semiconductor coupling faces two issues: choosing proper semiconductor components with suitable band structure, and projecting effective preparation methods to couple the components.

Graphitic carbon nitride (g-C₃N₄) is a polymeric semiconductor which consists of two earth-abundant elements (carbon and nitrogen), and easy to be prepared through thermal condensation of several low-cost nitrogen-rich precursors. It possesses a low band gap of 2.67 eV and relative more negative CB position of

¹School of Materials Science and Engineering, Yunnan University, 650091 Kunming, People's Republic of China.

²Department of Physics, Yunnan University, 650091 Kunming, People's Republic of China. ³Yunnan Province Key Lab of Micro-Nano Materials and Technology, Yunnan University, 650091 Kunming, People's Republic of China. Correspondence and requests for materials should be addressed to Y.D.W. (email: ydwang@ynu.edu.cn)

–1.1 eV^{13–15}. Such the band structure makes g-C₃N₄ suitable to form semiconductor coupling with both wide-band and visible-light semiconductors. For wide-band semiconductor, the narrow band gap of g-C₃N₄ induces better absorption of visible light, and the relative negative CB position guarantees the typical heterojunction charge transfer under visible light. For visible-light semiconductor, the relative more negative CB position results in a high possibility of forming Z-scheme charge transfer, and g-C₃N₄ acts as reduction site. Moreover, the polymeric nature of g-C₃N₄ endows sufficient flexibility which leads that g-C₃N₄ can serve as an anchoring support for various inorganic nanoparticles. Owing to these extraordinary characters, g-C₃N₄-based photocatalyst has gained increasing investigation which naturally includes g-C₃N₄-coupling photocatalysts, and several g-C₃N₄-based semiconductor coupling systems with enhanced photocatalytic activity have been reported^{16–18}. However, because the calcinations process is necessary in the preparation of g-C₃N₄, most of the reported literatures use two-step mechanical mixing or one-pot calcinations methods to prepare g-C₃N₄-coupling photocatalyst^{19–22}. Obviously, the aforementioned methods are hard to achieve a well-dispersed structure on the surface of g-C₃N₄, controlled particle size as well as fine tuning of the interface contact, which greatly hinder the catalytic performance²³. Considering the wide use of g-C₃N₄-coupling photocatalysts, it is meaningful to search a proper preparation method to obtain well-controlled morphology, especially a general approach through which a series of g-C₃N₄-coupling photocatalysts can be successfully prepared. To this task, one desire way is combining g-C₃N₄ with a well-investigated method which is a general route to nanostructure semiconductors.

When it comes to a general route to nanostructure semiconductors, the surfactant-free nonaqueous sol-gel methods that only involve organic solvents and metal organic precursors in the reaction system can not be ignored²⁴. Among the organic solvents used in surfactant-free nonaqueous methods, benzyl alcohol and its derivatives, first reported by Niederberger *et al.*, are the most brilliant^{25,26}. Through the versatile solvents, numerous semiconductors including nitrides^{27,28}, sulfides²⁹, binary and ternary oxides^{30,31} have been effectively synthesized. It covers most of the semiconductors used in heterogeneous photocatalysis. More importantly, its products are easy to be controlled in nanoscale, even smaller than 10 nm, with few aggregations, which is what we want in preparation of g-C₃N₄-coupling photocatalysts. On the other hand, Pinna's group found that graphene oxide is compatible with the “benzyl alcohol route”, and a series of graphene/metal oxide heterostructures like SnO₂³², Fe₃O₄³³, as well as TiO₂³⁴ based graphene heterostructures were obtained. For the obtained heterostructures, the oxide nanoparticles with ultrasmall size within 10 nm are uniformly anchored on the surface of reduction graphene oxide.

As we know, g-C₃N₄ possesses the similar layered structure with graphite. The layered g-C₃N₄ nanosheets could be also compatible with the “benzyl alcohol route”, which could be a general route to g-C₃N₄-coupling photocatalysts with controlled particle size as well as fine tuning of the interface contact. To our best knowledge, such the combination is still unreported. Meanwhile, TiO₂ is the first reported oxide through the “benzyl alcohol route”, and its preparation mechanism and size tuning method have been investigated in detail^{35–37}. Zhu *et al.* also reported that the TiO₂ obtained through such the “benzyl alcohol route” shows good photodegradation performance toward phenol³⁸. Choosing the mature components can greatly decrease the investigation difficulty in the compatibility.

Hence, this work uses g-C₃N₄/TiO₂ as the case to verify whether g-C₃N₄ is compatible with the “benzyl alcohol route” to fabricating g-C₃N₄-coupling photocatalysts. The crystal structure and morphology features of obtained g-C₃N₄/TiO₂ were fully characterized. The coupling sample shows double degradation efficiency of Rhodamine B under visible light than either g-C₃N₄ or TiO₂. Its Z-scheme enhanced mechanism was investigated through radical scavenger tests, X-ray photoelectron spectroscopy (XPS) and UV-vis spectrum. Moreover, a good performance including degradation efficiency and photocatalytic stability of the photocatalyst under sunlight was also observed.

Results and Discussion

Structure and morphology of as-prepared g-C₃N₄/TiO₂. The crystal structures of as-prepared samples were characterized by XRD, and the experimental data are shown in Fig. 1. For as-prepared pure g-C₃N₄, the curve exhibits a typical XRD pattern of g-C₃N₄, which consists of two characteristic peaks around 13.04° of (100) crystal plane, and 27.36° of (002) crystal plane^{39–41}, respectively. All the peaks of pattern b match well with the (101), (103), (004), (112), (200), (105) and (211) reflections of anatase-type TiO₂ (PDF No. 21-1272). The other patterns display the XRD curves of g-C₃N₄/TiO₂. Comparing them with that of TiO₂ and g-C₃N₄, one can find that the major peaks are identical to that of TiO₂, including the shape and position. It seems the relative amount of g-C₃N₄ is very low so that only a small peak at 27.36°, the (002) reflection of g-C₃N₄, is observed, as shown in Fig. 1(b). The results indicate that the added g-C₃N₄ does not influence the formation of TiO₂. On the other hand, it is observed that the peaks belonging to TiO₂ possess an observed diffraction widening, so as to the overlapping of some adjacent peaks, such as the overlapping of (103), (004) and (112) peaks. These phenomena imply the TiO₂ ought to have a small particles size which is an important parameter determining the photocatalytic activity. Rietveld refinement was used to have further revealing of the structural characters of TiO₂. The refined pattern together with the experimental data, Bragg position as well as difference curve are shown in Fig. S1. One can find that the black calculated pattern matches well with the experimental data and the difference curve only shows fluctuations, indicating that the calculated value is convinced. Through the refinement, the grain size of the TiO₂ is calculated to be 7.65 nm. Such the ultra-small particle size is identical to the reports of such the “benzyl alcohol route”. Apart from the grain size, the other structural parameters including the space group, cell parameters, atom coordinate as well as microstrain are listed in Table S1.

Due to the overlapping and widening of the peaks, the XRD peaks of g-C₃N₄ are undistinguished in the pattern of as-prepared g-C₃N₄/TiO₂. In this case, the FTIR was carried out to further confirm the structure of the g-C₃N₄/TiO₂, and the results are shown in Fig. 2. Compared with that of TiO₂, a series of peaks in the range of 1700–1200 cm^{−1} is easily observed in the pattern of g-C₃N₄, and belongs to the typical stretching modes of CN

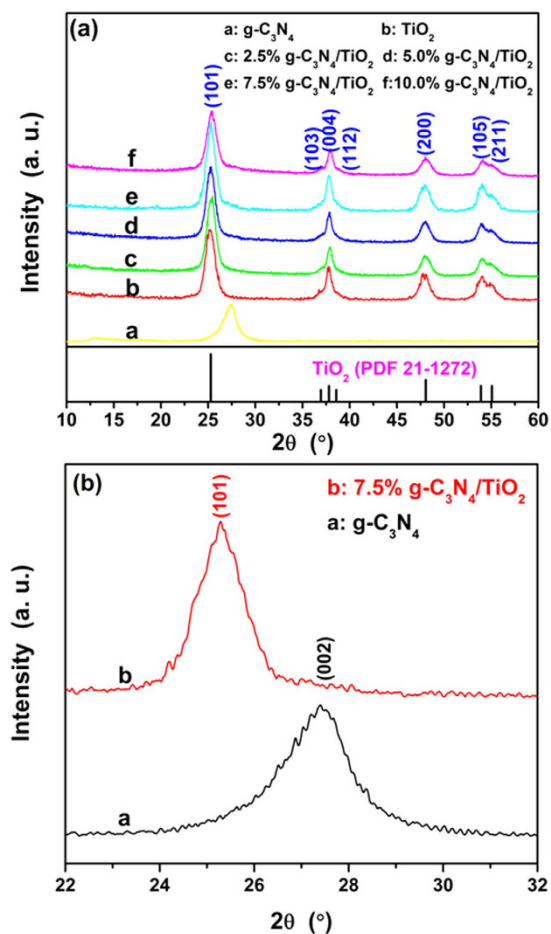


Figure 1. XRD patterns of (a) as-prepared samples and (b) enlarged view of the 22°–32° region.

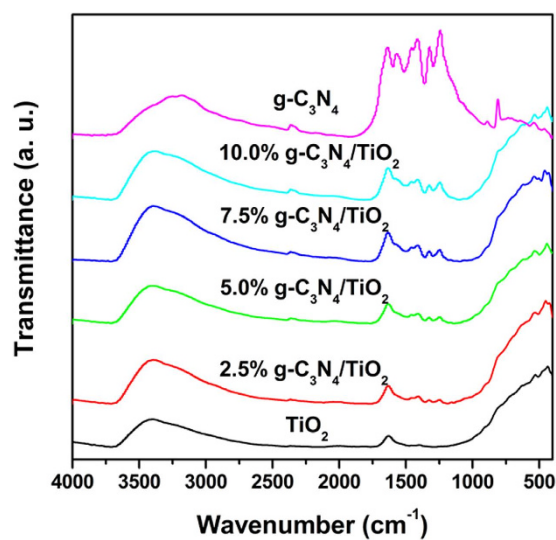


Figure 2. FTIR spectra of as-prepared samples.

heterocycles. These peaks are also can be found in the curves of $g\text{-C}_3\text{N}_4/\text{TiO}_2$ samples. Their intensity increases with the amount of $g\text{-C}_3\text{N}_4$. The results demonstrate that the structure of $g\text{-C}_3\text{N}_4$ is remained after the growth of TiO_2 .

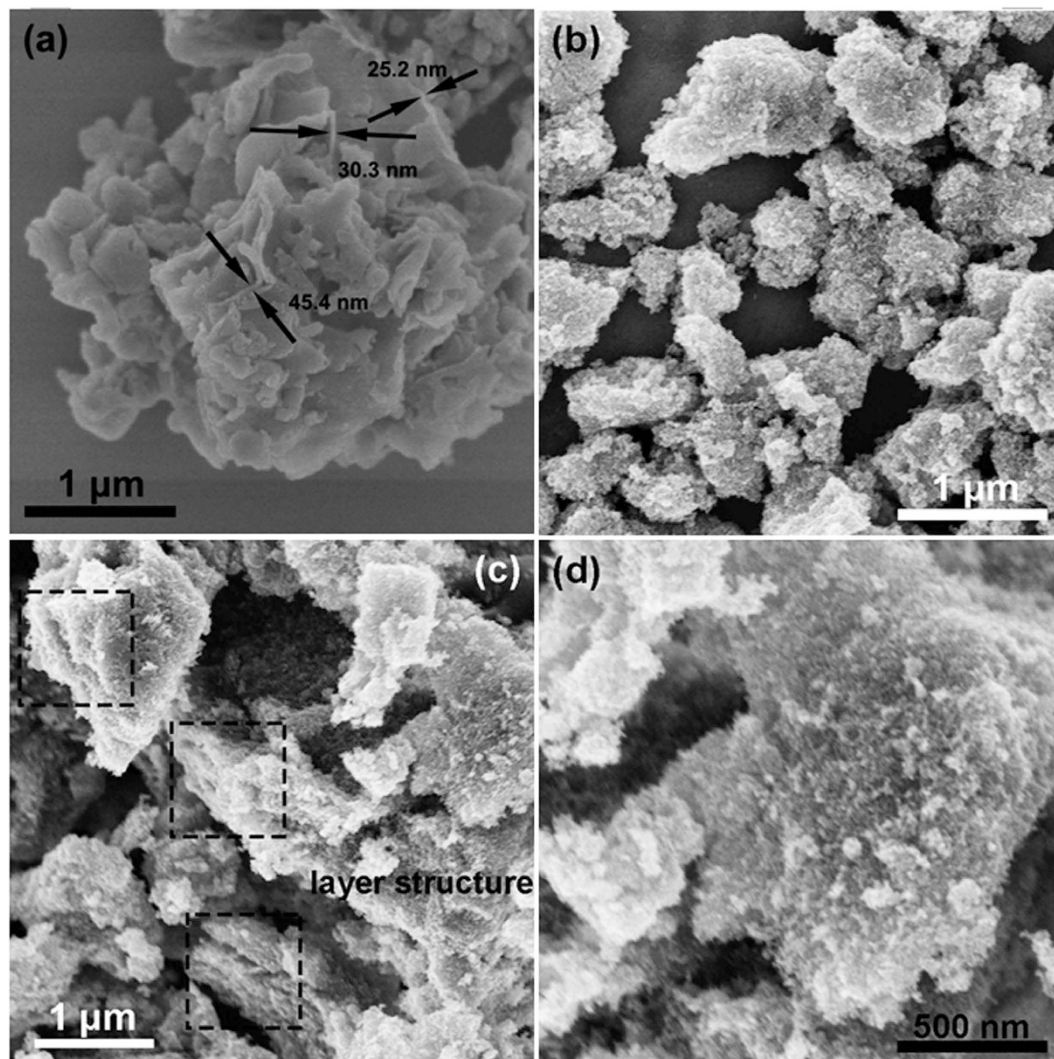


Figure 3. FESEM images of as-prepared samples. (a) $g\text{-C}_3\text{N}_4$, (b) TiO_2 , (c) and (d) 5% $g\text{-C}_3\text{N}_4/\text{TiO}_2$.

To observe the micro-morphology of as-prepared samples, FESEM was carried out. Figure 3(a) displays the morphology of $g\text{-C}_3\text{N}_4$. It can be seen that the $g\text{-C}_3\text{N}_4$ is made up of stacking nanosheets whose thickness is easy to be measured and falls in tens nanometers. The surface morphology of TiO_2 and 5% $g\text{-C}_3\text{N}_4/\text{TiO}_2$ is shown in Fig. 3(b) and (c) which have the same magnification as Fig. 3(a). In Fig. 3(b), several submicron-size aggregations of TiO_2 nanoparticles are observed. Under the same magnification, the morphology of $g\text{-C}_3\text{N}_4/\text{TiO}_2$ is different from that of $g\text{-C}_3\text{N}_4$ and TiO_2 . The surface of the composite is rough as that of TiO_2 , but the size of the composite is much larger than that of TiO_2 aggregations. For a better observation of the finer morphology, the surface of $g\text{-C}_3\text{N}_4/\text{TiO}_2$ is magnified and shown in Fig. 3(d). The finer structure consists of ultra-small particles. Combined the experimental section as well as the XRD results, it is believed that the ultra-small nanoparticles might belong to TiO_2 introduced by the benzyl alcohol reaction. Besides, the layered structure belonging to $g\text{-C}_3\text{N}_4$ is also can be seen in the region marked by square in Fig. 3(c). The results imply that the morphology may result from that the TiO_2 nanoparticles are tightly anchored on the surface of $g\text{-C}_3\text{N}_4$. The SEM images of 2.5%, 7.5% and 10% $g\text{-C}_3\text{N}_4/\text{TiO}_2$ are shown in Fig. S2. The similar morphology can be observed in all these samples.

To verify the point that the TiO_2 is anchored on the surface of $g\text{-C}_3\text{N}_4$, element mapping of the $g\text{-C}_3\text{N}_4/\text{TiO}_2$ is carried out and its results are shown in Fig. 4. Figure 4(a) displays the SEM image of the $g\text{-C}_3\text{N}_4/\text{TiO}_2$ composite whose edge shows the layered structure. As shown in Fig. 4(b,c,d) and (e), N, C, Ti, O uniformly distribute on the region of the composite, even in the edge region, which fully proves the prediction about the distribution of $g\text{-C}_3\text{N}_4$ and TiO_2 in the composite. In Fig. 4(f), it is also observed that the signal of Ti and O is much stronger than that of C and N. This phenomenon can be explained by the lower content of $g\text{-C}_3\text{N}_4$ in the composite.

Due to the limited magnification of SEM, the morphology of the anchored TiO_2 particles is not clear. Hence, TEM were carried out to gain a better understanding of the morphological and structural features. Figure 5(a) and (b) display the TEM images of $g\text{-C}_3\text{N}_4$ and 7.5% $g\text{-C}_3\text{N}_4/\text{TiO}_2$, respectively. Comparing these two figures, the similar results with that of FESEM can be observed. The $g\text{-C}_3\text{N}_4$ is made up of the stacking thin nanosheets whose surface is rather smooth. But it is clearly observed the surface of $g\text{-C}_3\text{N}_4$ is full of tens

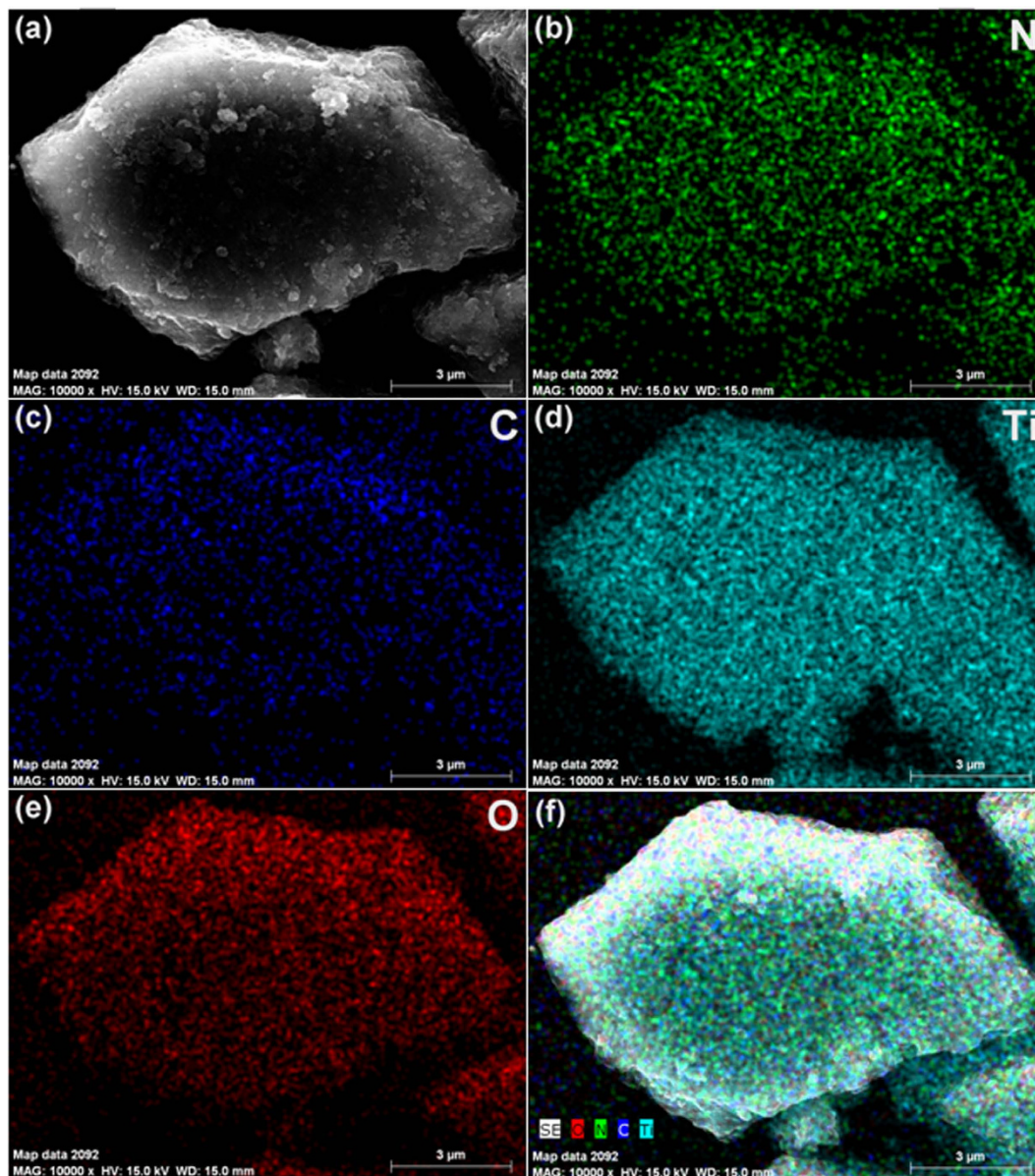


Figure 4. FESEM image of as-prepared $g\text{-C}_3\text{N}_4/\text{TiO}_2$ and corresponding EDX mapping images of N, C, Ti and O.

thousands of ultrasmall nanoparticles. With the selected-area electron-diffraction (SAED), a series of clear diffraction rings corresponding to the reflections (101), (004), (200) and (105) of anatase-type TiO_2 is observed in the inset, which further reveals that the anchored nanoparticles are polycrystal anatase TiO_2 . Figure 5(c) exhibits the magnified TEM image of $g\text{-C}_3\text{N}_4/\text{TiO}_2$. The well-defined TiO_2 nanoparticles are randomly anchored on the surface of $g\text{-C}_3\text{N}_4$, and no hard aggregation is observed between the nanoparticles. The tight combination between $g\text{-C}_3\text{N}_4$ and TiO_2 is favorable to charge transfer between these two semiconductors which possess the proper band structure. While the uniform and isolated distribution of the TiO_2 nanoparticles is beneficial for exposing more active site for the heterogeneous catalysis. The inset displays the HRTEM image of one isolated TiO_2 nanoparticle. The clear fringes make it easy to estimate the interplanar spacing which is 0.353 nm and corresponding to the (101) plane of anatase. On the other hand, since the anchored nanoparticles show a well-defined morphology, the grain size of these particles are obtained by measuring the size of five hundreds particles, and the results are shown in Fig. 5(d). The result, 7.3 ± 1.6 nm, matches well with refinement of XRD. Both of them indicate that the TiO_2 on the surface of $g\text{-C}_3\text{N}_4/\text{TiO}_2$ prepared through the “benzyl alcohol route” possesses an ultrasmall particle size.

With the XRD, FTIR, FESEM, element mapping and TEM toward the as-prepared samples, it is sure that $g\text{-C}_3\text{N}_4$ is compatible with the “benzyl alcohol route” in the term of crystal structure and morphology. The addition of $g\text{-C}_3\text{N}_4$ does not disturb the chemical reactions and crystallization in the nonaqueous sol-gel route based on benzyl alcohol. Moreover, the formed TiO_2 nanoparticles with ultrasmall grain size are uniformly anchored

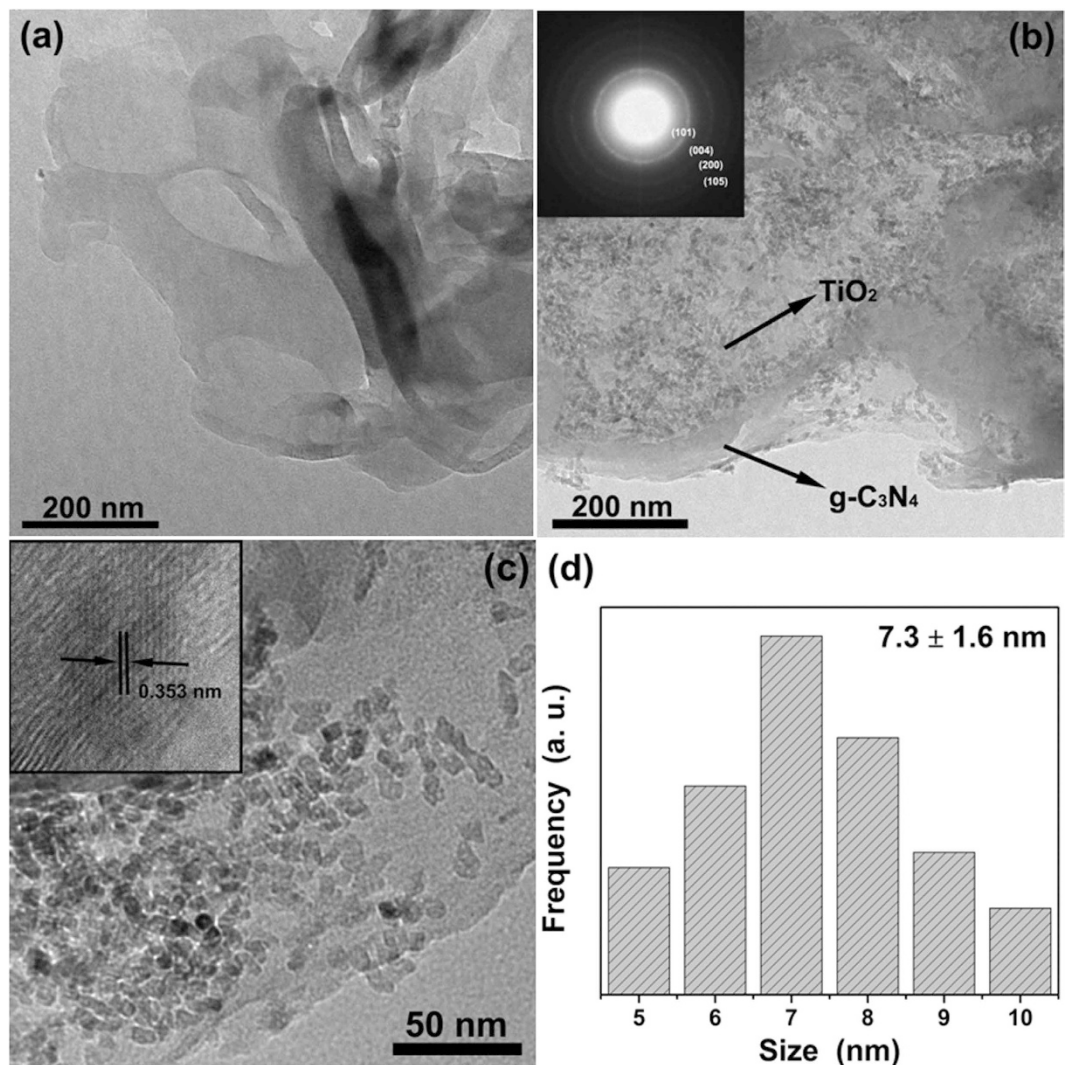


Figure 5. TEM images of as-prepared (a) $g\text{-C}_3\text{N}_4$ and (b) 7.5% $g\text{-C}_3\text{N}_4/\text{TiO}_2$. (c) Magnified TEM image of as-prepared $g\text{-C}_3\text{N}_4/\text{TiO}_2$. (d) Grain size distribution of TiO_2 nanoparticles anchored on the surface of $g\text{-C}_3\text{N}_4$. The insets of (b) and (c) correspond to the SAED pattern of 7.5% $g\text{-C}_3\text{N}_4/\text{TiO}_2$ and HRTEM of one isolated TiO_2 nanoparticle anchored on the surface of $g\text{-C}_3\text{N}_4$, respectively.

on the surface of $g\text{-C}_3\text{N}_4$ without hard aggregations in a wide range. Such the scenario is exactly what we want and seldom reported before. And such the good combination of TiO_2 and $g\text{-C}_3\text{N}_4$ can be attributed three main reasons: (1) the “benzyl alcohol route” gives the TiO_2 a very small particle size; (2) the electronegativity of the $g\text{-C}_3\text{N}_4$ nanosheets endows a strong electrostatic adsorption of Ti^{4+} , which leads to a further tight combination⁴²; (3) more importantly, $g\text{-C}_3\text{N}_4$ nanosheets possesses very good compatible with the “benzyl alcohol route” like the GO does.

Photocatalytic properties of as-prepared $g\text{-C}_3\text{N}_4/\text{TiO}_2$ under visible light. It has been proved that $g\text{-C}_3\text{N}_4$ is compatible with the “benzyl alcohol route” to prepare $g\text{-C}_3\text{N}_4/\text{TiO}_2$ nanocomposites from the aspects of structure and morphology. In this section, the photocatalytic properties of as-prepared $g\text{-C}_3\text{N}_4/\text{TiO}_2$ under visible light are evaluated. And RhB, a typical organic dye which is a common water pollutant and could cause long-term environmental toxicity and short-term public health damage^{43–45}, is chosen as the model pollutant. Prior the irradiation under the light source, half hour dark treatment was carried out to realize adsorption equilibrium and eliminate the influence of adsorption on degradation. Figure 6 shows the evolution of degradation rate along with the time. All the curves have a similar linear downtrend which seems to be zero-order kinetic process. Hence, the data points after the dark treatment were fitted according to the zero-order kinetic process:

$$C/C_0 = -kt + b \quad (1)$$

where k is the degradation rate constant, and b represents the residual composition at 0 h. The k , b , and R^2 values of the fitted curves for all samples are listed in Table 1. Firstly, all the R^2 values higher than 0.9842 indicating the fitted curves match well with the obtained data, and the degradation surely follows the zero-order kinetic process.

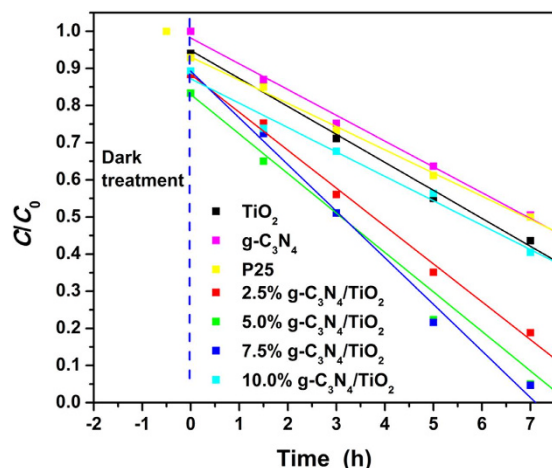


Figure 6. Photocatalytic activity plots of as-prepared samples for degradation of RhB under visible light.

Sample	b	k (h^{-1})	R^2
TiO ₂	0.9484	0.0753	0.9910
2.5% g-C ₃ N ₄ /TiO ₂	0.8841	0.1021	0.9948
5.0% g-C ₃ N ₄ /TiO ₂	0.8297	0.1139	0.9942
7.5% g-C ₃ N ₄ /TiO ₂	0.8924	0.1255	0.9920
10.0% g-C ₃ N ₄ /TiO ₂	0.8720	0.0656	0.9842
g-C ₃ N ₄	0.9820	0.0694	0.9936
P25	0.9308	0.0628	0.9970

Table 1. The k , b and R^2 values following the zero-order kinetic process.

Secondly, the as-prepared g-C₃N₄/TiO₂ nanocomposites show higher degradation rate constant than both TiO₂ and g-C₃N₄, and even the commercial P25 photocatalyst, which demonstrates a high photocatalytic activity of as-prepared g-C₃N₄/TiO₂ nanocomposites. The compounding of g-C₃N₄ and TiO₂ through combining g-C₃N₄ and “benzyl alcohol route” is meaningful. Thirdly, the composite containing 7.5% g-C₃N₄ displays the highest k value, which means 7.5% is the best ratio of g-C₃N₄ in the presented preparation method. On the other hand, the b in the fitted equation can reflect the adsorption ability of the photocatalyst, because it represents the residual composition at 0 h and after dark treatment. From the listed b values in Table 1, the as-prepared g-C₃N₄/TiO₂ nanocomposites have the lower value than as-prepared g-C₃N₄ and TiO₂. Such the stronger adsorption ability can be understood from the FESEM and TEM images. The morphology that the ultrasmall TiO₂ nanoparticles uniformly anchored on the surface of g-C₃N₄ prevents the aggregations of TiO₂ and increase the surface roughness of g-C₃N₄. But for the g-C₃N₄/TiO₂ with different content of g-C₃N₄, the values of b are random which indicates that the enhanced activity is not only resulted from the better adsorption. For example, the sample with 7.5% g-C₃N₄ possesses the best degradation efficiency, but its b value is the highest among the other samples of g-C₃N₄/TiO₂. Hence, it is believed that there are some other reasons leading to the enhanced activity apart from the better adsorption. In the introduction, it is predicted that the coupling of g-C₃N₄ and wide-band semiconductor could result in a better utilization of visible light, and separation as well as transfer of photogenerated carries. All of them could enhance the visible-light driven photocatalysis activity.

Mechanisms of the enhanced photocatalytic activities of g-C₃N₄/TiO₂. In this section, the mechanisms of the enhanced photocatalytic activities of g-C₃N₄/TiO₂ were studied from the adsorption, utilization of visible light, and charge transfer, respectively.

In usual, a better adsorption is linked to a higher specific surface area⁴⁶, so the N₂ adsorption-desorption experiments toward the as-prepared TiO₂, g-C₃N₄ and g-C₃N₄/TiO₂ were carried out. Since the content of g-C₃N₄ is relative low, and there are four samples with different content, the 10% g-C₃N₄/TiO₂ with highest amount of g-C₃N₄ was chosen as the example to make the results clearer and easier to be analyzed. The isotherms and corresponding pore size distribution curves are shown in Fig. 7. In the similar isotherms of TiO₂ and g-C₃N₄/TiO₂, the evident hysteresis loops from 0.5 to 0.9 can be observed, indicating the presence of mesopores within the materials. This can be further verified from the pore size distribution curves. The TiO₂ and g-C₃N₄/TiO₂ show the pores centered at 7.211 and 6.15 nm, respectively. According to the shape of the hysteresis loops and the TEM results, the observed mesoporous is resulted from the accumulation of TiO₂ nanoparticles. The isotherm of g-C₃N₄ also shows non-closed and porous character as shown in the Fig. 7 and its inset. But its specific surface area is much lower than that of TiO₂ and g-C₃N₄/TiO₂. To be more specific, the value from BET measurement of TiO₂, g-C₃N₄/TiO₂

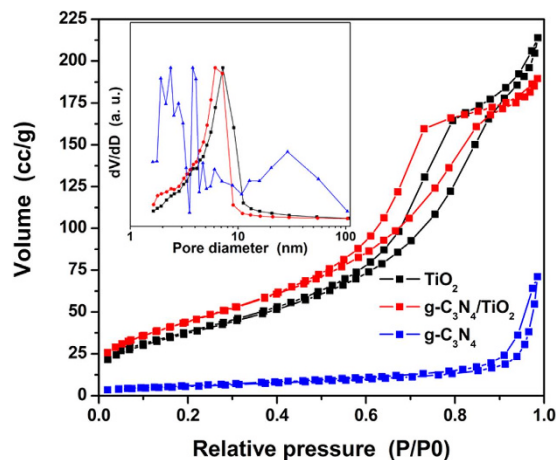


Figure 7. N_2 adsorption-desorption isotherms of as-prepared TiO_2 , $g-C_3N_4$ as well as $g-C_3N_4/TiO_2$, and the corresponding normalized pore-size distribution (inset).

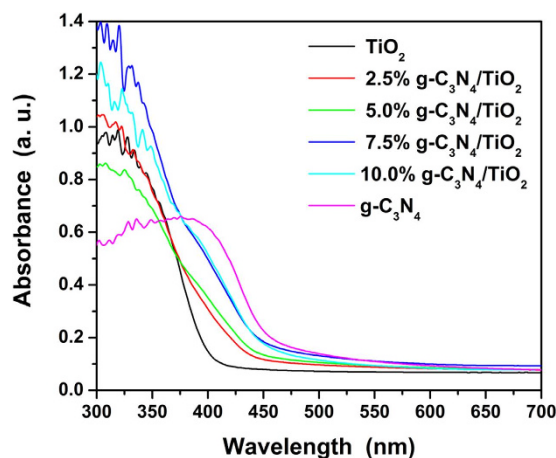


Figure 8. UV-vis spectra of as-prepared samples.

and $g-C_3N_4$ are 141, 166 and $21 \text{ m}^2 \text{ g}^{-1}$, respectively. These results well prove the prediction made from the b values listed in Table 1.

Figure 8 displays the UV-vis spectra of as-prepared samples. The curve of TiO_2 displays an absorption edge in ultraviolet region, which corresponds to the band gap of TiO_2 . But the as-prepared TiO_2 still shows some absorption in visible light. Such the absorption backs the visible-light driven photocatalytic activity of TiO_2 . Due to the narrower band gap of $g-C_3N_4$ (2.67 eV), the edge absorption of $g-C_3N_4$ arise at the region with longer wavelength than TiO_2 . Comparing the curves of $g-C_3N_4/TiO_2$ with that of TiO_2 , one can find a better absorption of visible light from 400 to 550 nm which matches well with the spectra of $g-C_3N_4$, and the absorption is increased with the content of $g-C_3N_4$. Hence, it is clear that $g-C_3N_4$ enhances the visible-light utilization of TiO_2 , owing to the narrower band gap of 2.67 eV.

It is generally accepted that the photoluminescence (PL) spectra can be used to check the separation and transfer of photogenerated carriers⁴⁷. Due to the separation and transfer, the recombination of the photogenerated carriers are decreased, which further leads to reduced PL of the coupling. However, for the coupling of $g-C_3N_4$ and TiO_2 , such the method loses its function. Because the $g-C_3N_4$ shows very strong PL which even can be observed by naked eyes, but PL intensity of TiO_2 is much lower. Hence, the composite shows stronger PL than TiO_2 , but lower PL than $g-C_3N_4$, as shown in Fig. S3. Such the result matches with other reported literatures^{23,48,49}. In this situation, the photoelectrochemical measurement was carried out to verify the separation of the photogenerated carriers. Figure 9(a) displays the transient photocurrent responses of TiO_2 , $g-C_3N_4$ and their composite through typical switch on-off cycles^{50–52}. It is observed all the materials show fast response and recovery. And the composite shows the highest current, followed by TiO_2 . The lowest current of $g-C_3N_4$ may be attributed to the high recombination of the photogenerated carriers which can be understood from Fig. S3. The highest photocurrent directly proves the separation of photogenerated carriers in $g-C_3N_4/TiO_2$. By the way, the electrochemical impedance spectroscopy (EIS) was carried out and its results are shown in Fig. 9(b). From the figure, the arc character of all samples can be observed. It is reported that the charge lifetime is related to the recombination resistance, and large semicircle radius of EIS curves implies large recombination resistance^{53–55}. From the obtained EIS curves,

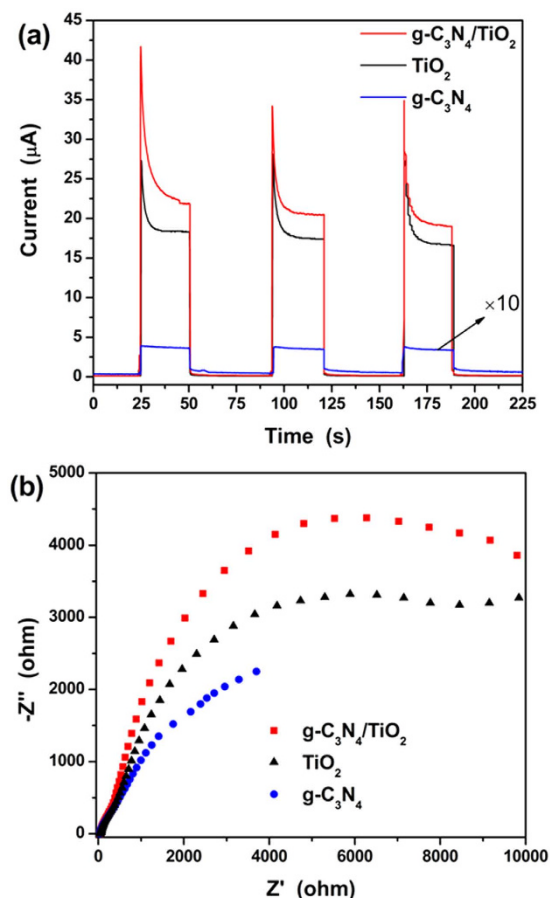


Figure 9. Photoelectrochemical measurement of TiO_2 , $\text{g-C}_3\text{N}_4$, and $\text{g-C}_3\text{N}_4/\text{TiO}_2$ composite. (a) transient photocurrent responses and (b) EIS Nyquist plots.

one can find that the $\text{g-C}_3\text{N}_4/\text{TiO}_2$ has the largest radius, while the $\text{g-C}_3\text{N}_4$ possesses the smallest. The results match well with that of photocurrents. From the photoelectrochemical measurement, it is known that the combination of $\text{g-C}_3\text{N}_4$ and TiO_2 increase the recombination resistance and lifetime of photogenerated carries, which is resulted from the charge separation.

On the other hand, it is known to us that the reactive species trapping experiment is effective in judgment of active species. Further step, the mode of carries transfer as well as separation could be indirectly studied. Hence, it was carried out to study the possible separation and transfer of photogenerated carries. In this work, ethylenediamine teracetic acid disodium salt (EDTA-2Na, 0.01 M), *p*-benzoquinone (BZQ, 0.001 M) and isopropanol (IPA, 0.02 M) were used as scavengers for photogenerated holes, superoxide anion radicals and hydroxyl radicals, respectively^{56,57}. The removal rates of the dye at 7 h with different catalysts were used for comparison. Because the behaviors of the composite highly depend on its components, and the function of the conduction band and valence band directly influence the judgment of the charge transfer model, the behavior of two components, TiO_2 and $\text{g-C}_3\text{N}_4$, are firstly studied.

Figure 10(a) displays the results of TiO_2 . Without any trapping reagent, the as-prepared TiO_2 shows the ability of breaking down the RhB dye under visible light. With addition of the sacrifice reagents, the removal rates of the dye decrease, which means photogenerated holes, superoxide anion radicals and hydroxyl radicals are produced and active during the degradation process. Especially the active photogenerated holes exclude the dye-sensitization mechanism of the degradation, because the hole is not involved in the dye-sensitization process⁵⁸. However, it is generally accepted that the band gap of anatase-type TiO_2 is 3.2 eV which is too wide to produce photogenerated carries and consequent corresponding redox reactions. But the result of the trapping reagents indirectly proves the existence of aforementioned process. For these, we attribute these to the possibly existing oxygen vacancies in the TiO_2 nanoparticles. Nakamura *et al.* created oxygen vacancies in TiO_2 by plasma treatment to increase its photocatalytic activities under visible light, and brought out that the oxygen vacancies facilitate visible light absorption by generating discrete state below the conduction band of TiO_2 ⁵⁹. Ihara *et al.* also reported that oxygen vacancies can be easily created in the grain boundaries⁶⁰. In this work, the TiO_2 nanoparticles anchored on the surface of $\text{g-C}_3\text{N}_4$ have a very small grain size, and they are easy to form varies defects on their surface, naturally include the oxygen vacancy. It is believed that the oxygen-related defects including the oxygen vacancy can be indirectly observed in the O1s XPS spectra in the form of absorbed oxygen ion. To verify the existence of the absorbed oxygen ion, XPS toward TiO_2 and 7.5% $\text{g-C}_3\text{N}_4/\text{TiO}_2$ were carried out. The magnified O1s XPS spectra are shown in Fig. S4(a) and (b), respectively. The peak with lower binding energy

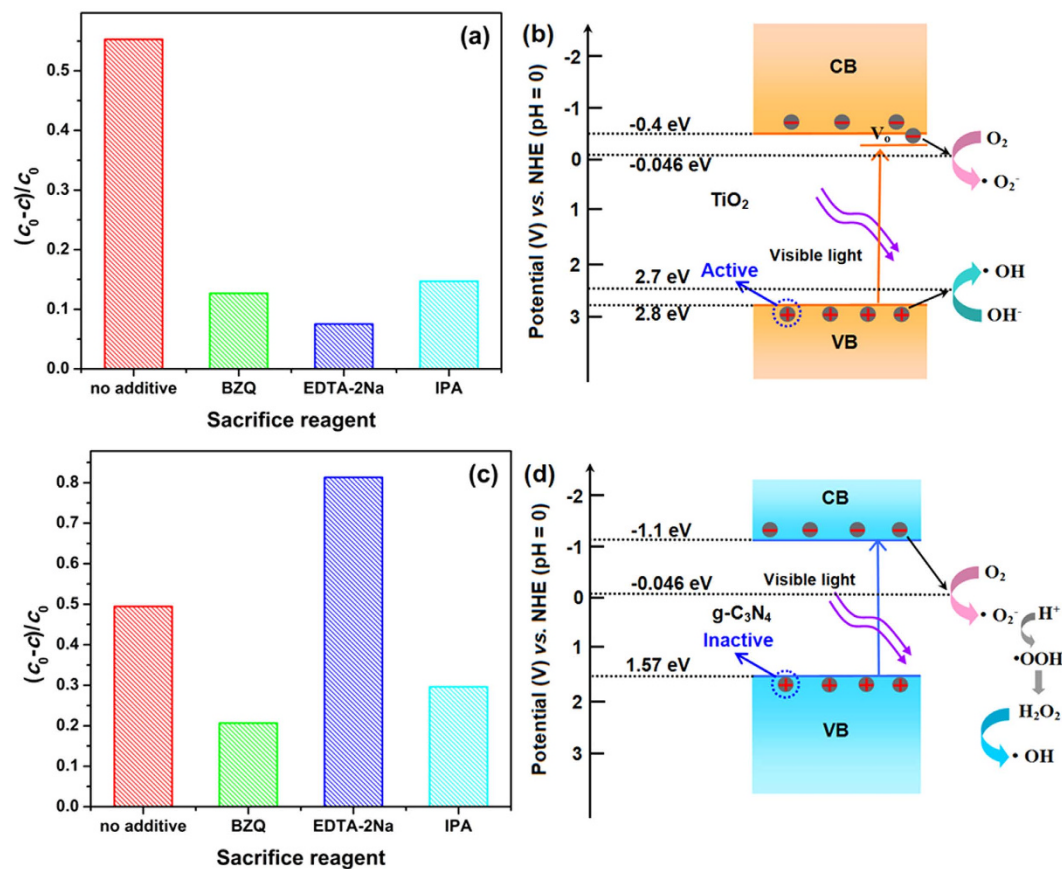


Figure 10. Reactive species trapping experiments of as-prepared (a) TiO₂ and (c) g-C₃N₄. The degradation mechanisms of as-prepared (b) TiO₂ and (d) g-C₃N₄. The pillars in (a) and (c) show the removal rate of the dye at 7 h.

around 530 eV is associated to the oxygen atom in the crystal lattice, while the peak with higher binding energy is assigned to the absorbed oxygen ion⁶¹. It proves that there surely exist the oxygen related defects including the oxygen vacancy. And it also forebodes that the TiO₂ in the g-C₃N₄/TiO₂ could also show the similar photocatalytic behaviors to the pure TiO₂. Based on the oxygen vacancy introducing defect level and the results of sacrifice reagent, the degradation mechanism of as-prepared TiO₂ under visible light is obtained as shown in Fig. 10(b).

Unlike wide-band TiO₂, g-C₃N₄, a visible-light semiconductor with a narrow band gap of 2.67 eV, is easy to be excited by visible light. Its result of trapping experiments is shown in Fig. 10(c). Two unusual phenomena are observed, including that the addition of hole trapping reagent (EDTA-2Na) intensively increases the removal rate, and the hydroxyl radical arises and show its function in the degradation process. The active species in the degradation process can be predicted through comparing the top of valence band (TVB) potential and bottom of conduction band (BCB) potential with the standard redox potential (SRP) of corresponding reactions. Since the E_{BCB} and E_{TVB} of g-C₃N₄ have been widely studied, -1.10 eV and 1.57 eV are adopted to be the E_{BCB} and E_{TVB} , respectively¹⁶. Also, it is known to us that the SRP of O₂/ \cdot O₂⁻ and OH⁻/ \cdot OH are -0.046 and +2.7 V vs. NHE, respectively¹². Due to the E_{BCB} of g-C₃N₄ is more negative than the SRP of O₂/ \cdot O₂⁻, the photogenerated electrons can react with O₂ to form \cdot O₂⁻. But the E_{TVB} of g-C₃N₄ is lower than the SRP of OH⁻/ \cdot OH, so \cdot OH can not be formed through the reaction of photogenerated holes and OH⁻. Although the photogenerated holes can not produce \cdot OH, it is believed the generated holes still can oxidize the pollutant. So, it is generally accepted that the effective species during the photocatalysis reaction of g-C₃N₄ are holes, and \cdot O₂⁻^{62,63}. According to the result shown in Fig. 10(c), the prediction can not explain the behavior of the g-C₃N₄ for the degradation of RhB. Therefore, the effect of the conduction band and valence band of g-C₃N₄ need further analysis. As we know, the potential of TVB and BCB decides the redox ability of the photogenerated carriers. More negative BCB means stronger reduction photogenerated electrons, and more positive TVB means stronger oxidation photogenerated holes. The g-C₃N₄ possesses very negative BCB, but its TVB is weak. Hence, the oxidation ability of the photogenerated hole is weak which makes the hole show few effects on the RhB molecules just like the hole can not react with OH⁻ to form \cdot OH. Moreover, the excess photogenerated holes would recombine with the photogenerated electrons which can form the effective \cdot O₂⁻ species. Especially, the g-C₃N₄ always shows a strong blue photoluminescence, indicating a strong recombination of the photogenerated carriers. With the addition of EDTA-2Na, the trapping reagent of photogenerated holes, the inactive holes are consumed, and the reduced amount of generated holes decreases the recombination possibility of photogenerated carriers. That is to say, more photogenerated electrons are kept on the conduction band, so the removal rate is increased. On the other hand, due to the strong reduction of the

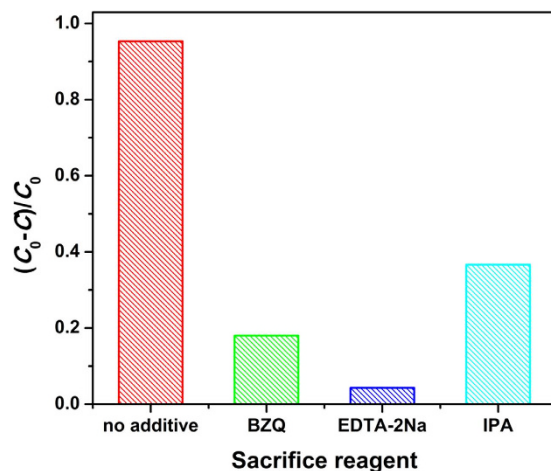


Figure 11. Reactive species trapping experiments of as-prepared 7.5% g-C₃N₄/TiO₂. The pillars show the removal rate of the dye at 7 h.

photogenerated electrons, the formed $\cdot\text{O}_2^-$ also possesses very strong reduction which could lead to the further reactions and formation of $\cdot\text{OH}$ radicals through an intermediate of $\cdot\text{OOH}$ ^{64,65}. That is why the addition of IPA, $\cdot\text{OH}$ trapping reagent, causes the lower removal rate. Hence, the degradation mechanism of g-C₃N₄ toward RhB solution is summarized in Fig. 10(d). From the trapping experiments toward TiO₂ and g-C₃N₄, it is found that the most difference between them during the degradation process under visible light in the aspect of effective species is that the photogenerated holes in the valence band of TiO₂ is active, but inactive for g-C₃N₄. Such the conclusion is different from the common reported literatures in which the difference is thought to be whether there are OH⁻ species according to the comparison of calculated potential of BCB and TVB with the SRP of corresponding reactions^{21,49,63}. At the same time, the conclusion is very important to the analysis of charge transfer model and mechanism of enhanced photocatalytic activity of g-C₃N₄/TiO₂ nanocomposite. Hence, the analysis of trapping experiments also should be based on the experiments of its components rather than simple theoretical comparisons.

The active species trapping experiments toward 7.5% g-C₃N₄/TiO₂ are carried out, and the results are shown in Fig. 11. Generally speaking, all three tested species including photogenerated hole, superoxide anion radical and hydroxyl radical are active during the photocatalysis process. Comparing with Fig. 10(a) and (c), one can find that the active species of the composite are different from that of g-C₃N₄, but similar to that of TiO₂. Further step, the removal rates are normalized according to the removal rate with no additive. For pure TiO₂, the normalized removal rates with BZQ, EDTA-2Na and IPA are 22.91%, 13.60%, and 26.59%, respectively. For 7.5% g-C₃N₄/TiO₂, the normalized removal rates with BZQ, EDTA-2Na and IPA are 18.90%, 4.48%, and 38.45%, respectively. It is clear that the experimental data between TiO₂ and 7.5% g-C₃N₄/TiO₂ are distinguished, and it also could not be the simple superposition of g-C₃N₄ and TiO₂. Especially for the removal rate with EDTA-2Na, the photogenerated hole is effective for TiO₂, and inactive for g-C₃N₄. While for their composite it shows a stronger effect than that for TiO₂. Hence, the degradation model of g-C₃N₄/TiO₂ is different from their components, which is resulted from the separation and transfer of the photogenerated carriers.

On the other hand, according to the degradation mechanism of TiO₂ (Fig. 10(b)) and g-C₃N₄ (Fig. 10(d)), the two possible separation and transfer models of carriers for g-C₃N₄/TiO₂ nanocomposite are shown in Fig. 12(a) and (b), which correspond to typical heterojunction and Z-scheme charge transfer models, respectively. Comparing these two models, one can find that the active species in the Z-scheme model are photogenerated hole, superoxide anion radical and hydroxyl radical, but the active species of heterojunction-type model only involves superoxide anion radical. For the heterojunction-type model, although it is not sure whether the superoxide anion radicals generated in the conduction band of TiO₂ can produce hydroxyl radical, it is certain that the holes formed in the valence band of g-C₃N₄ are inactive. Comparing this certain difference between the two models with the experimental data, it can be concluded that the separation and transfer model of as-prepared g-C₃N₄/TiO₂ is Z-scheme. Through the Z-scheme, the different behaviors of g-C₃N₄/TiO₂ and TiO₂ can be explained. The superoxide anion radical is generated on the conduction band of g-C₃N₄ whose E_{BCB} is more negative than that of TiO₂. With stronger reduction, the effect of superoxide anion radical is enhanced compared with TiO₂. Although the valence band is the place forming the active holes for both TiO₂ and g-C₃N₄/TiO₂, there is a lower possibility of carrier recombination of g-C₃N₄/TiO₂ than TiO₂ due to the Z-scheme charge transfer in g-C₃N₄/TiO₂. For hydroxyl radical, it is formed through the photogenerated holes on the valence band of TiO₂. Since the photogenerated holes are directly consumed by the dye molecules in g-C₃N₄/TiO₂, the residual holes for generation of hydroxyl radical are decreased. Hence, the effect of hydroxyl radical is decreased for g-C₃N₄/TiO₂. Through the trapping experiments, it proves the Z-scheme charge transfer between g-C₃N₄ and TiO₂ in g-C₃N₄/TiO₂. And the enhanced activity with the Z-scheme charge transfer can be attributed to the consequent stronger reduction ability of the material, and effective charge separation.

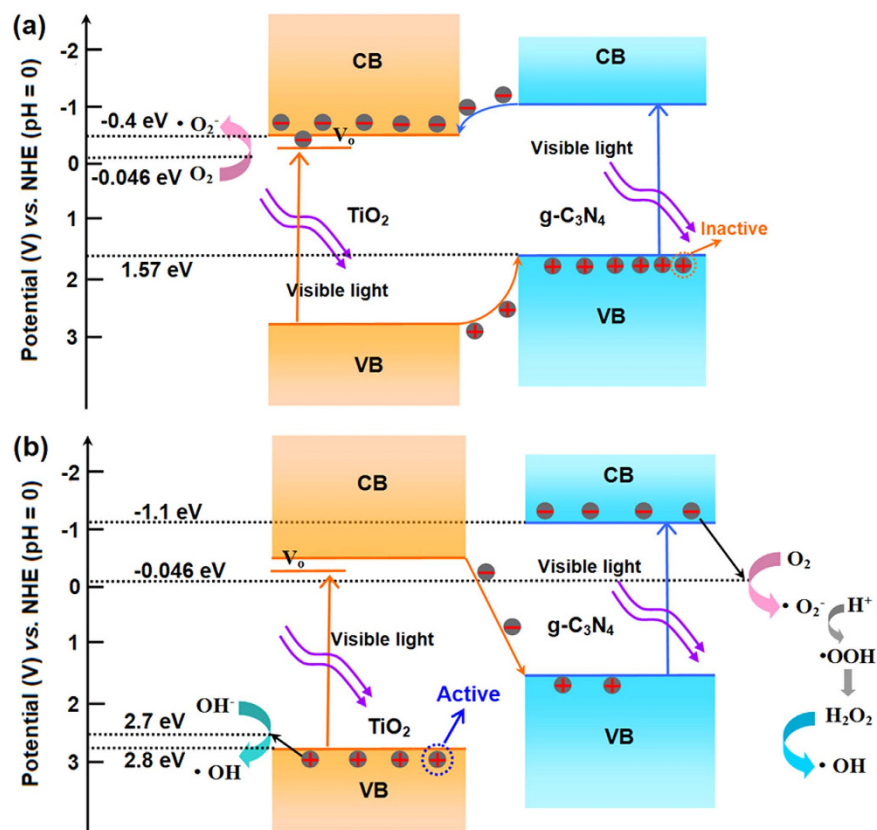


Figure 12. The degradation mechanisms of as-prepared $g\text{-C}_3\text{N}_4/\text{TiO}_2$ in the form of (a) typical heterojunction and (b) Z-scheme.

Hence, the enhanced photocatalytic activity of $g\text{-C}_3\text{N}_4/\text{TiO}_2$ under visible light is resulted from the increased adsorption, better utilization of visible light, Z-scheme charge transfer as well as consequent stronger reduction ability toward the dye molecules.

Photocatalytic performances of as-prepared $g\text{-C}_3\text{N}_4/\text{TiO}_2$ under sunlight. In order to test the potential of $g\text{-C}_3\text{N}_4/\text{TiO}_2$ in practical application, the photocatalytic performances of as-prepared $g\text{-C}_3\text{N}_4/\text{TiO}_2$ nanocomposites under sunlight are tested. Because the 7.5% is the optimal content of $g\text{-C}_3\text{N}_4$, 7.5% $g\text{-C}_3\text{N}_4/\text{TiO}_2$ was chosen as the object.

Figure 13 displays the evolution of degradation rate along with the time. It is observed that the data points in the blank group fluctuates around 1, indicating that the degradation caused by the sunlight can be neglected during the test. With the addition of 7.5% $g\text{-C}_3\text{N}_4/\text{TiO}_2$, the concentration of the RhB is decreased rapidly. It only takes 40 min to remove 96.37% RhB. 99.5% RhB was broken down at 1 h. Such the removal efficiency is about ten times faster than that under visible light. On the other hand, de-ethylation of RhB is always observed in its photodegradation, and the de-ethylation process could lead to the shift of absorption peak from 550 to 500 nm, and consequent decrease of absorbance at its initial position of absorption peak⁶⁶. But the de-ethylation only takes a small part of the whole of degradation process, and double time is usually needed. In this term, the UV-vis spectra of the centrifuged solutions were tested and shown in Fig. 13(b). It is observed that the strong absorption peak has no shift during the degradation reaction. That is to say the rapid degradation of RhB pollutant is not resulted from the de-ethylation. Hence, the as-prepared 7.5% $g\text{-C}_3\text{N}_4/\text{TiO}_2$ certainly possesses quite high photocatalytic activity. And the inset shows the photo of the centrifuged solutions. The color of the solution fades along with the time, and turns to be colorless and transparent solution. While the higher efficiency can be attributed to the different light resource: the first, the sunlight is much stronger than the 24 W lamp used as the visible-light resource; there are some ultraviolet in the sunlight, which is beneficial for exciting more carriers for TiO_2 component.

As we know, the photocatalytic stability of the catalysts is one of the most important parameter evaluating the possibility of practical application. Hence the degradation evolution in five cycles of degradation tests under sunlight was recorded as shown in Fig. 14. Unexpectedly, the photocatalyst not only keep a good stability, but also has a better efficiency with the increase of the cycle time. The degradation rate reaches higher than 99% for all the cycles at 60 min. At 25 min, the degradation rate reaches 83.77%, 89.55%, 94.48%, 97.40% and 99.02% for first, second, third, fourth and fifth cycle, respectively. Because the property is always associated with the microstructure of the catalysts, the TEM toward the catalyst after the 5 cycles was carried out, and shown in Fig. S5. In the Fig. S5, the composite of the sheet-like $g\text{-C}_3\text{N}_4$ and ultras-small TiO_2 nanoparticles are still observed. But the amount of the TiO_2 nanoparticles loaded on the surface of $g\text{-C}_3\text{N}_4$ is much smaller than the primary sample

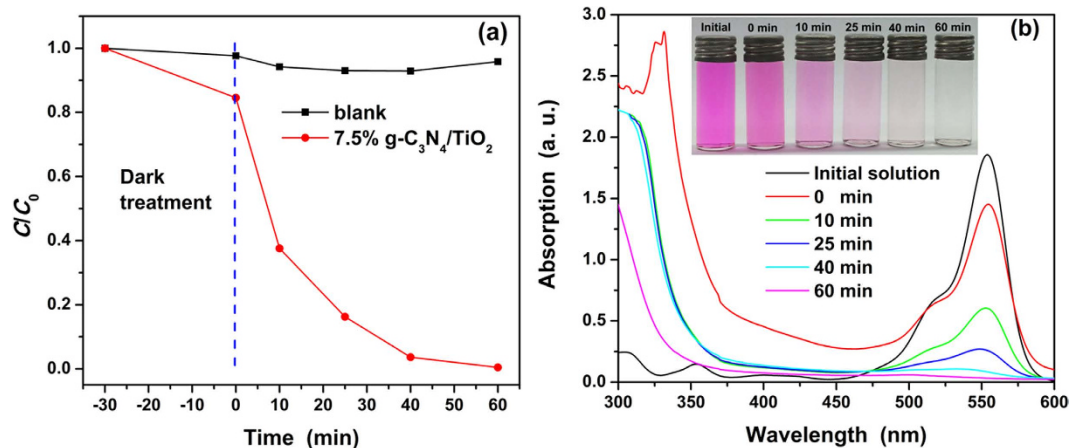


Figure 13. (a) Photocatalytic activity plots of as-prepared 7.5% g-C₃N₄/TiO₂ for degradation of RhB under sunlight. (b) UV-vis spectra of the centrifuged solutions at different degradation time. Inset is the photo the centrifuged solutions.

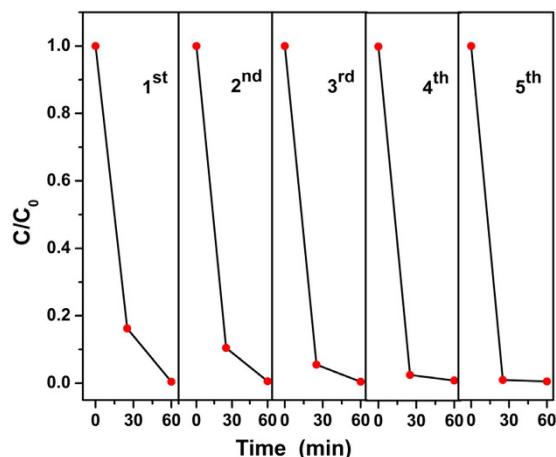


Figure 14. Repeated photocatalytic experiments of 7.5% g-C₃N₄/TiO₂ for five times under irradiation of sunlight.

shown in Fig. 5(b). The degradation efficiency is increased with the decreased amount of TiO₂ loaded on the surface of g-C₃N₄ according to the results of TEM and stability tests. And Fig. 6 and Table 1 have proved that 7.5% is the best ratio amount 0, 2.5%, 5.0%, 7.5% and 10.0%. Hence, the contradiction arises. Such the unusual phenomenon might be explained through the presented experiment details. In the preparation experiment, TiO₂ is the matrix, and its amount is constant. The g-C₃N₄ is used as enhancer, and its amount is calculated according to the mass ratio of g-C₃N₄/TiO₂. Such the design of the experiment ignores that although the g-C₃N₄ is compatible with benzyl alcohol, its dispersed amount is limited. The amount of g-C₃N₄ added in the preparation of 7.5% g-C₃N₄/TiO₂ could be the maximum. With further addition of g-C₃N₄, it stacks with each other, and the exposed surface is limited for TiO₂ to attach. Hence, 7.5% is the best in the projecting experiments. But the optimal ratio should be much higher than 7.5% so that the catalyst's efficiency increases along with smaller loaded TiO₂ nanoparticles. From this point of view, it suggests that the g-C₃N₄ should be used as the matrix or the baseline to calculate the amount of the other components. And the limited dispersing amount of g-C₃N₄ can be improved through decrease the thick of the g-C₃N₄ nanosheets, which also could make the "benzyl alcohol route" more economic and the products more active. Anyhow, it has proven g-C₃N₄ is compatibility with the benzyl-alcohol-based non-aqueous sol-gel route, and the combination could be a general route to g-C₃N₄-coupling photocatalysts with controlled morphology and enhanced photocatalytic activity.

Conclusions

Through the combination of g-C₃N₄ and classical nonaqueous sol-gel route based on benzyl alcohol, g-C₃N₄/TiO₂ coupling photocatalysts were obtained. Owing to the contribution of benzyl-alcohol-based nonaqueous sol-gel route, the TiO₂ on the surface of g-C₃N₄ shows ultrasmall grain size. Due to the excellent compatibility of g-C₃N₄ and the benzyl alcohol route, the TiO₂ nanoparticles are uniformly distributed on the surface of g-C₃N₄. For the present experimental parameters, the optimal mass ratio of g-C₃N₄/TiO₂ is 7.5%. And the enhanced photocatalytic activity under visible light is attributed to the Z-scheme heterojunction, and consequent better absorption

of visible light, enhanced reduction ability as well as decreased recombination. The as-prepared $g\text{-C}_3\text{N}_4/\text{TiO}_2$ also has high efficiency and good cycle performance under sunlight, indicating its practical application. Through the detailed study of as-prepared $g\text{-C}_3\text{N}_4/\text{TiO}_2$ and considering that “benzyl alcohol route” is one general route to numerous size-controlled photocatalysts, it is believed that such the nonaqueous sol-gel route could be a general method to $g\text{-C}_3\text{N}_4$ -coupling photocatalysts with desired morphology and contact interface.

Methods

Materials and synthesis. All the chemical reagents used in the experiments were obtained from commercial sources as guaranteed-grade reagents and used without further purification.

Well-defined $g\text{-C}_3\text{N}_4$ nanostructure was synthesized through thermal condensation of cyanuric acid-melamine complex⁶⁷. Briefly, 6.45 g grinded cyanuric acid was added to 100 mL ethanol with stirring. 6.3 g melamine was then grinded and added to the above suspension. The mixture was continuing stirred for 8 h, and then dried at 60 °C. The obtained white powder was subsequently calcined at 550 °C under N_2 atmosphere for 4 h with a heating rate of 2.3 °C min^{-1} to gain the final $g\text{-C}_3\text{N}_4$ powder.

The $g\text{-C}_3\text{N}_4/\text{TiO}_2$ nanocomposites were *in-situ* prepared on the pre-synthesized nanostructured $g\text{-C}_3\text{N}_4$ through the “benzyl alcohol route”. Firstly, 10 mL xylol was poured into a closed conical flask, and then 0.69 mL TiCl_4 was dissolved with magnetic stirring. Five minutes later, 66 mL benzyl alcohol was gently poured into the system. After stirring for another five minutes, the calculated amount of pre-synthesized $g\text{-C}_3\text{N}_4$ was further grinded and added to the titanium precursor solution. The amount of $g\text{-C}_3\text{N}_4$ was calculated according to mass ratios of $g\text{-C}_3\text{N}_4/\text{TiO}_2 = 0\%$, 2.5%, 5.0%, 7.5% as well as 10%, respectively. The corresponding samples were named as TiO_2 and $x\%$ $g\text{-C}_3\text{N}_4/\text{TiO}_2$ ($x = 2.5, 5.0, 7.5, 10.0$), respectively. To gain a better dispersing of $g\text{-C}_3\text{N}_4$ and promote the adsorption of Ti^{4+} on the $g\text{-C}_3\text{N}_4$ surface with electronegativity, the mixtures were treated with ultrasound for 2 h. Later, with further stirring for 30 s, 70 mL of the homogeneous precursors were transferred into the Teflon-lined stainless steel autoclaves with a capacity of 83 mL and reacted at 180 °C for only 4 h, respectively. The autoclaves were cooled down to room temperature, and the resulting precipitates were washed with ethanol for four times and dried at 60 °C overnight.

Characterization of as-prepared samples. X-ray diffraction (XRD, Rigaku D/MAX-3B powder diffractometer) with a copper target and K_α radiation ($\lambda = 1.54056 \text{ \AA}$) was used for the phase identification, where the diffracted X-ray intensities were recorded as a function of 2θ . The samples were scanned from 10° to 80° (2θ) in steps of 0.02°. Fourier transformed infrared (FTIR) spectra were recorded on AVATAR 360 FT-IR spectrophotometer. The microstructures of the samples were tested on Hitachi S-4800 field emission electron microscopy (FESEM) with the energy dispersive X-ray (EDX) device. The transmission electron micrographs (TEM) were obtained with a Zeiss EM 912 Ω instrument at an acceleration voltage of 120 kV, while high-resolution transmission electron microscopy (HRTEM) characterizations were carried out using a Philips CM200-FEG microscope (200 kV, $C_s = 1.35 \text{ mm}$). The samples used for TEM were prepared by dispersing the products in ethanol with ultrasound treatment, and the dispersion was then dropped on carbon-copper grids. The nitrogen adsorption-desorption technique was measured at 77.3 K with Autosorb iQ Station 1. Prior to the measurement, the sample was degassed at 300 °C for 28.4 h under a vacuum situation. UV-vis measurements were made with a Hitachi U4100 spectrophotometer with a wavelength range between 300 to 700 nm. Photoluminescence (PL) spectra were made with a FLS 980 spectrophotometer of Edinburgh Instruments. X-ray photoelectron spectroscopy (XPS) was carried out at room temperature in ESCALAB 250 system. During XPS analysis, an Al K_α X-ray beam was adopted as the excitation source and the vacuum pressure of the instrument chamber was $1 \times 10^{-7} \text{ Pa}$ as read on the panel. Measured spectra were decomposed into Gaussian components by a least-square fitting method. Bonding energy was calibrated with reference to C1s peak (285.0 eV).

Evaluation of the photocatalytic activity of the samples. Since the strong absorption peaks in the visible light, which is favorable the direct evaluation, Rhodamine B (RhB, $\text{C}_{28}\text{H}_{31}\text{ClN}_2\text{O}_3$) is chosen as the model pollutant and indicator of the photocatalytic activity in this work. The photocatalytic properties under visible light of the prepared sample were evaluated with a 24 W visible-light lamp as light source, and the light below 400 nm was removed using a glass filter. In a typical degradation test, 40 mg of the as-synthesized sample was added into a quartz beaker with addition of 50 mL RhB solution (10 mg/L). The distance between the lamp and the solution surface was 6 cm. The dispersion (6 mL) was extracted and centrifuged to separate the catalyst and dye solution at 8500 rev. per min for 10 min at different intervals. The changed RhB concentration of the centrifuged solutions was recorded using a UV-1800 spectrophotometer according to Beer-Lambert’s Law. The UV-vis spectra of the centrifuged solution were also measured using the UV-1800 spectrophotometer from 300 to 600 nm. The photocatalytic performances under sunlight of the $g\text{-C}_3\text{N}_4/\text{TiO}_2$ were tested through the similar procedures. For the photocatalytic performance of the $g\text{-C}_3\text{N}_4/\text{TiO}_2$ under sunlight, except that sunlight was directly used as the light source, all other processes are similar with that of visible-light tests. And all the sunlight tests were carried out in sunny days in March 2016 between 11 am and 14 pm in Kunming, China.

Photoelectrochemical measurements of the samples. The photoelectrochemical measurements were performed on CHI660E (Chenhua Instrument, Shanghai, China) in a neutral aqueous system (0.1 M Na_2SO_4) using a three-electrode system. A platinum (Pt) plate and a saturated calomel electrode (SCE, 0.2415 V vs SHE) were used as the counter and the reference electrode, respectively. Light source is provided by 8 W UV lamp (Spectroline EA-180/FE). The working electrode was prepared as follows: 20 mg of the sample was dispersed in 20 mL ethanol with ultrasound for 30 min; 5 μL of the mixture was dropt to an ITO glass ($1.25 \times 2.5 \text{ cm}^2$); then the electrode was obtained after drying at 60 °C for 1 h and sintering at 300 °C for 1 h.

References

- Cao, S. W. *et al.* g-C₃N₄-based photocatalysts for hydrogen generation. *J. Phys. Chem. Lett.* **5**, 2101–2107 (2014).
- Fu, J. W. *et al.* Dual Z-scheme charge transfer in TiO₂-Ag-Cu₂O composite for enhanced photocatalytic hydrogen generation. *J. Mater. Chem.* **1**, 124–133 (2015).
- Akple, M. S. *et al.* Enhanced visible light photocatalytic H₂-production of g-C₃N₄/WS₂ composite heterostructures. *Appl. Surf. Sci.* **358**, 196–203 (2015).
- Jin, J. *et al.* A hierarchical Z-Scheme CdS-WO₃ photocatalyst with enhanced CO₂ reduction activity. *Small* **11**, 5262–5271 (2015).
- Yu, W. L. *et al.* Enhanced photocatalytic activity of g-C₃N₄ for selective CO₂ reduction to CH₃OH via facile coupling of ZnO: a direct Z-scheme mechanism. *J. Mater. Chem. A* **3**, 19936–19947 (2015).
- Yu, J. G. *et al.* Enhanced photocatalytic performance of direct Z-scheme g-C₃N₄-TiO₂ photocatalysts for the decomposition of formaldehyde in air. *Phys. Chem. Chem. Phys.* **15**, 16883–16890 (2013).
- Liu, Y. N. *et al.* Enhanced visible-light photocatalytic activity of Z-scheme graphitic carbon nitride/oxygen vacancy-rich zinc oxide hybrid photocatalysts. *Chinese J. Catal.* **36**, 2135–2144 (2015).
- Zhu, C. S. *et al.* Fabrication of Z-scheme Ag₃PO₄/MoS₂ composites with enhanced photocatalytic activity and stability for organic pollutant degradation. *Appl. Surf. Sci.* **377**, 99–108 (2016).
- Xiao, D. *et al.* Hydrothermal synthesis of α-Fe₂O₃/g-C₃N₄ composite and its efficient photocatalytic reduction of Cr(VI) under visible light. *Appl. Surf. Sci.* **358**, 181–187 (2015).
- Huang, S. T. *et al.* Z-scheme TiO₂/g-C₃N₄ composites with improved solar-driven photocatalytic performance deriving from remarkably efficient separation of photo-generated charge pairs. *Mater. Res. Bull.* **84**, 65–70 (2016).
- Dong, G. H. *et al.* Efficient anoxic pollutant removal with oxygen functionalized graphitic carbon nitride under visible light. *RSC Adv.* **4**, 5553–5560 (2014).
- Zhou, P. *et al.* All-solid-state Z-scheme photocatalytic systems. *Adv. Mater.* **26**, 4920–4935 (2014).
- Cao, S. W. *et al.* Polymeric photocatalysts based on graphitic carbon nitride. *Adv. Mater.* **27**, 2150–2176 (2015).
- Ye, S. *et al.* A review on g-C₃N₄ for photocatalytic water splitting and CO₂ reduction. *Appl. Surf. Sci.* **358**, 15–27 (2015).
- Wen, J. Q. *et al.* A review on g-C₃N₄-based photocatalysts. *Appl. Surf. Sci.* **391**, 72–123 (2017).
- Hong, Y. Z. *et al.* In-situ synthesis of direct solid-state Z-scheme V₂O₅/g-C₃N₄ heterojunctions with enhanced visible light efficiency in photocatalytic degradation of pollutants. *Appl. Catal. B: Environ.* **180**, 663–673 (2016).
- Pan, C. S. *et al.* Dramatic activity of C₃N₄/BiPO₄ photocatalyst with core/shell structure formed by self-assembly. *Adv. Funct. Mater.* **22**, 1518–1524 (2012).
- Yu, J. G. *et al.* Noble metal-free Ni(OH)₂-g-C₃N₄ composite photocatalyst with enhanced visible-light photocatalytic H₂-production activity. *Catal. Sci. Technol.* **3**, 1782–1789 (2013).
- Pany, S. *et al.* A facile *in situ* approach to fabricate N, S-TiO₂/g-C₃N₄ nanocomposite with excellent activity for visible light induced water splitting for hydrogen evolution. *Phys. Chem. Chem. Phys.* **17**, 8070–8077 (2015).
- Zhou, J. W. *et al.* Photocatalytic enhancement of hybrid C₃N₄/TiO₂ prepared via ball milling method. *Phys. Chem. Chem. Phys.* **17**, 3647–3652 (2015).
- Liao, W. J. *et al.* Synthesis of Z-scheme g-C₃N₄-Ti³⁺/TiO₂ material: an efficient visible light photoelectrocatalyst for degradation of phenol. *Phys. Chem. Chem. Phys.* **17**, 8877–8884 (2015).
- Xu, J. *et al.* g-C₃N₄ modified TiO₂ nanosheets with enhanced photoelectric conversion efficiency in dye-sensitized solar cells. *J. Power Sources* **274**, 77–84 (2015).
- Li, H. *et al.* In situ growth of TiO₂ nanocrystals on g-C₃N₄ for enhanced photocatalytic performance. *Phys. Chem. Chem. Phys.* **17**, 17406–17412 (2015).
- Wang, C. *et al.* Synthesis of nanocrystalline TiO₂ in alcohols. *Powder Technol.* **125**, 39–44 (2002).
- Niederberger, M. *et al.* Benzyl alcohol and transition metal chlorides as a versatile reaction system for the nonaqueous and low-temperature synthesis of crystalline nano-objects with controlled dimensionality. *J. Am. Chem. Soc.* **124**, 13642–13643 (2002).
- Niederberger, M. *et al.* Organic reaction pathways in the nonaqueous synthesis of metal oxide nanoparticles. *Chem. Eur. J.* **12**, 7282–7302 (2006).
- Buha, J. *et al.* Thermal transformation of metal oxide nanoparticles into nanocrystalline metal nitrides using cyanamide and urea as nitrogen source. *Chem. Mater.* **19**, 3499–3505 (2007).
- Deshmukh, R. *et al.* Ultrasmall Cu₃N nanoparticles: surfactant-free solution-phase synthesis, nitridation mechanism, and application for lithium storage. *Chem. Mater.* **27**, 8282–8288 (2015).
- Ludi, B. *et al.* Extension of the benzyl alcohol route to metal sulfides: “nonhydrolytic” thio sol-gel synthesis of ZnS and SnS₂. *Chem. Commun.* **47**, 5280–5282 (2011).
- Pinna, N. *et al.* Surfactant-free nonaqueous synthesis of metal oxide nanostructures. *Angew. Chem. Int. Ed.* **47**, 5292–5304 (2008).
- Shi, N. *et al.* Facile synthesis of monodisperse Co₃O₄ quantum dots with efficient oxygen evolution activity. *Chem. Commun.* **51**, 1338–1340 (2015).
- Russo, P. A. *et al.* Room-temperature hydrogen sensing with heteronanostructures based on reduced graphene oxide and tin oxide. *Angew. Chem. Int. Ed.* **51**, 11053–11057 (2012).
- Baek, S. *et al.* A one-pot microwave-assisted non-aqueous sol-gel approach to metal oxide/graphene nanocomposites for Li-ion batteries. *RSC Adv.* **1**, 1687–1690 (2011).
- Russo, P. A. *et al.* Microwave-assisted coating of carbon nanostructures with titanium dioxide for the catalytic dehydration of D-xylose into furfural. *RSC Adv.* **3**, 2595–2603 (2013).
- Jensen, G. V. *et al.* Anisotropic crystal growth kinetics of anatase TiO₂ nanoparticles synthesized in a nonaqueous medium. *Chem. Mater.* **22**, 6044–6055 (2010).
- Niederberger, M. *et al.* Benzyl alcohol and titanium tetrachloride a versatile reaction system for the nonaqueous and low-temperature preparation of crystalline and luminescent titania nanoparticles. *Chem. Mater.* **14**, 4364–4370 (2002).
- Niederberger, M. *et al.* Tailoring the surface and solubility properties of nanocrystalline titania by a nonaqueous *in situ* functionalization process. *Chem. Mater.* **16**, 1202–1208 (2004).
- Zhu, J. *et al.* Nanocrystalline anatase TiO₂ photocatalysts prepared via a facile low temperature nonhydrolytic sol-gel reaction of TiCl₄ and benzyl alcohol. *Appl. Catal. B: Environ.* **76**, 82–91 (2007).
- Dong, G. H. *et al.* Carbon self-doping induced high electronic conductivity and photoreactivity of g-C₃N₄. *Chem. Commun.* **48**, 6178–6180 (2012).
- Dong, G. H. *et al.* Porous structure dependent photoreactivity of graphitic carbon nitride under visible light. *J. Mater. Chem.* **22**, 1160–1166 (2012).
- Zhu, B. C. *et al.* Fabrication and photocatalytic activity enhanced mechanism of direct Z-scheme g-C₃N₄/Ag₂WO₄ photocatalyst. *Appl. Surf. Sci.* <http://dx.doi.org/10.1016/j.apsusc.2016.07.104> (2016).
- Zhu, B. C. *et al.* Isoelectric point and adsorption activity of porous g-C₃N₄. *Appl. Surf. Sci.* **344** 188–195 (2015).
- Xu, L. L. *et al.* Nano-MnO_x on activated carbon prepared by hydrothermal process for fast and highly efficient degradation of azo dyes. *Appl. Catal. A: Gen.* **485**, 91–98 (2014).
- Chen, W. *et al.* In situ fabrication of novel Z-scheme Bi₂WO₆ quantum dots/g-C₃N₄ ultrathin nanosheets heterostructures with improved photocatalytic activity. *Appl. Surf. Sci.* **355**, 379–387 (2015).

45. Zhou, D. T. *et al.* In-situ construction of all-solid-state Z-scheme g-C₃N₄/TiO₂ nanotube arrays photocatalyst with enhanced visible-light-induced properties. *Sol. Energ. Mat. Sol. C.* **157**, 399–405 (2016).
46. Wen, J. Q. *et al.* Photocatalysis fundamentals and surface modification of TiO₂ nanomaterials. *Chinese J. Catal.* **36**, 2049–2070 (2015).
47. Liu, H. R. *et al.* Worm-like Ag/ZnO core-shell heterostructural composites: fabrication, characterization, and photocatalysis. *J. Phys. Chem. C* **116**, 16182–16190 (2012).
48. Ma, J. Z. *et al.* Enhanced photocatalytic oxidation of NO over g-C₃N₄-TiO₂ under UV and visible light. *Appl. Catal. B: Environ.* **184**, 28–34 (2016).
49. Li, Y. L. *et al.* Seed-induced growing various TiO₂ nanostructures on g-C₃N₄ nanosheets with much enhanced photocatalytic activity under visible light. *J. Hazard. Mater.* **292**, 79–89 (2015).
50. Lv, J. L. *et al.* Facile synthesis of Z-scheme graphitic-C₃N₄/Bi₂MoO₆ nanocomposite for enhanced visible photocatalytic properties. *Appl. Surf. Sci.* **358**, 377–384 (2015).
51. Li, J. Q. *et al.* Improved photoelectrochemical performance of Z-scheme g-C₃N₄/Bi₂O₃/BiPO₄ heterostructure and degradation property. *Appl. Surf. Sci.* **385**, 34–41 (2016).
52. Luo, J. *et al.* Rational construction of Z-scheme Ag₂CrO₄/g-C₃N₄ composites with enhanced visible-light photocatalytic activity. *Appl. Surf. Sci.* **390**, 357–367 (2016).
53. Han, J. H. *et al.* AgSbS₂ modified ZnO nanotube arrays for photoelectrochemical water splitting. *Appl. Catal. B: Environ.* **179**, 61–68 (2015).
54. Wu, W. Q. *et al.* Multistack intergration of three-dimensional hyperbranched anatase titania architectures for high-efficiency dye-sensitized solar cells. *J. Am. Chem. Soc.* **136**, 6437–6445 (2014).
55. Hsu, S. C. *et al.* Modulation of photocarrier dynamics in indoline dye-modified TiO₂ nanorod array/P3HT hybrid solar cell with 4-tert-butylpyridine. *J. Phys. Chem. C* **116**, 25721–25726 (2012).
56. Wang, Y. J. *et al.* Enhancement of photocurrent and photocatalytic activity of ZnO hybridized with graphite-like C₃N₄. *Energy Environ. Sci.* **4**, 2922–2929 (2011).
57. Xu, D. F. *et al.* Enhanced photocatalytic activity and stability of Z-scheme Ag₂CrO₄-GO composite photocatalysts for organic pollutant degradation. *Appl. Catal. B: Environ.* **164**, 380–388 (2015).
58. Rehman, S. *et al.* Strategies of making TiO₂ and ZnO visible light active. *J. Hazard. Mater.* **170**, 560–569 (2009).
59. Isao, N. *et al.* Role of oxygen vacancy in the plasma-treated TiO₂ photocatalyst with visible light activity for NO removal. *J. Mol. Catal. A: Chem.* **161**, 205–212 (2000).
60. Ihara, T. *et al.* Visible-light-active titanium oxide photocatalyst realized by an oxygen-deficient structure and by nitrogen doping. *Appl. Catal. B: Environ.* **42**, 403–409 (2003).
61. Chen, N. *et al.* Xylene sensing performance of WO₃ decorated anatase TiO₂ nanoparticles as a sensing material for gas sensor at low operating temperature. *RSC Adv.* **6**, 49692–49701 (2016).
62. Kumar, S. *et al.* Cost-effective and eco-friendly synthesis of novel and stable N-doped ZnO/g-C₃N₄ core-shell nanoplates with excellent visible-light responsive photocatalysis. *Nanoscale* **6**, 4830–4842 (2014).
63. Jo, W. K. *et al.* Influence of TiO₂ morphology on the photocatalytic efficiency of direct Z-scheme g-C₃N₄/TiO₂ photocatalysts for isoniazid degradation. *Chem. Eng. J.* **281**, 549–565 (2015).
64. Moon, J. *et al.* Photocatalytic activation of TiO₂ under visible light using Acid Red 44. *Catal. Today* **87**, 77–86 (2003).
65. Zhao, J. C. *et al.* Photocatalytic degradation of organic pollutants under visible light irradiation. *Top. Catal.* **35**, 269–278 (2005).
66. Liu, X. *et al.* One-step nonaqueous sol-gel route to mixed-phase TiO₂ with enhanced photocatalytic degradation of Rhodamine B under visible light. *CrystEngComm* **18**, 1964–1975 (2016).
67. Shalom, M. *et al.* Improving carbon nitride photocatalysis by supramolecular preorganization of monomers. *J. Am. Chem. Soc.* **135**, 7118–7121 (2013).

Acknowledgements

This work was supported by National Natural Science Foundation of China (Grant No.51262029), the Program for Excellent Young Talents, Yunnan University, Scientific Research Foundation of Yunnan Provincial Education Department (2016YJS002).

Author Contributions

The research was planned by Y.D.W. Experiments were performed by X.L., N.C. and Y.X.L. X.L. and Y.D.W. prepared the manuscript. D.Y.D. and X.X.X. involved in the scientific discussions. All the authors participated in discussing and reviewing of the manuscript.

Additional Information

Supplementary information accompanies this paper at <http://www.nature.com/srep>

Competing financial interests: The authors declare no competing financial interests.

How to cite this article: Liu, X. *et al.* A general nonaqueous sol-gel route to g-C₃N₄-coupling photocatalysts: the case of Z-scheme g-C₃N₄/TiO₂ with enhanced photodegradation toward RhB under visible-light. *Sci. Rep.* **6**, 39531; doi: 10.1038/srep39531 (2016).

Publisher's note: Springer Nature remains neutral with regard to jurisdictional claims in published maps and institutional affiliations.



This work is licensed under a Creative Commons Attribution 4.0 International License. The images or other third party material in this article are included in the article's Creative Commons license, unless indicated otherwise in the credit line; if the material is not included under the Creative Commons license, users will need to obtain permission from the license holder to reproduce the material. To view a copy of this license, visit <http://creativecommons.org/licenses/by/4.0/>

© The Author(s) 2016